1 **Apportionment and Inventory Comparison of Agriculture and Energy Sector Methane**
2 **Emissions using Multi-month Trace Gas Measurements in Northern Colorado**
3

4 **Griffin J. Mead,[1] Daniel I. Herman,[1,2] Fabrizio R. Giorgetta,[1,2] Nathan A. Malarich,[1]**
5 **Esther Baumann,[1,2] Brian R. Washburn,[1,2] Nathan R. Newbury,[1] Ian Coddington,[1] Kevin**
6 **C. Cossel[1,*]**
7

8 [1] National Institute of Standards and Technology, Spectrum Technology and Research Division,
9 Boulder, CO 80305

10 [2] University of Colorado, Boulder, Department of Physics, Boulder, CO 80309

11 Corresponding author: Kevin Cossel (kevin.cossel@nist.gov)

12

13 **Key Points:**

14 - Optimized methane fluxes across multiple sectors in a complex emissions environment
15   using a mid-infrared dual-comb spectrometer and tracer gas analysis

16 - Comparison with energy-sector inventory indicates decrease in emissions factors since
17   2012

18 - Comparison with agriculture-sector inventories emphasize the importance of spatial
19   distributions in regional comparisons

20 **Abstract**

21 Quantifying sector-resolved methane fluxes in complex emissions environments is challenging
22 yet necessary for inventory validations. We separate energy and agriculture sector methane
23 using a dynamic linear model of methane, ethane, and ammonia mixing ratios measured at a
24 Northern Colorado site from November 2021 to January 2022. Combining observations with
25 spatially resolved inventories and inverse methods, energy and agriculture methane fluxes are
26 constrained across a ~850 km^2 area. Optimized energy sector fluxes were 22% lower than the
27 inventory despite a ~360% increase in regional energy production since the inventory was
28 constructed, suggesting a regional decline in emissions factors. In contrast, optimized agriculture
29 fluxes were 3× larger than the inventory; we demonstrate this discrepancy is consistent with the
30 spatial distribution of agricultural sources. These results highlight the utility of sector-
31 apportioned methane observations for multi-sector inventory optimization in complex
32 environments, which may prove valuable for national and global quatification of sector-resolved
33 methane fluxes.

34

35 **Plain Language Summary**

36 Knowledge of the locations, fluxes, and kinds of methane sources is important for implementing
37 effective emissions mitigation technologies and regulations. Methane emissions are often
38 challenging to categorize because a wide variety of sources can emit methane, and these
39 disparate sources are often intermingled at relevant spatial scales. We demonstrate how a
40 dynamic linear model can use multi-month time series of two trace gases, ethane and ammonia,

41 to effectively separate methane into energy and agriculture source sectors. We demonstrate how
42 the sector-apportioned methane can be incoroporated into a Bayesian inversion approach for
43 refinement of these inventories. Our results suggest that emissions factors for energy
44 infrastructure have decreased three-fold since 2012 in the study area, and that our methodology
45 is sensitive to the spatial distribution of methane sources in the region.

46

1 Introduction

48   Increased use of hydrocarbons and the expansion of agriculture over the past century has
49 significantly increased atmospheric methane concentrations. While short-lived in the
50 atmosphere, methane has a global warming potential 24-28× that of carbon dioxide on a 100-
51 year timescale. International attempts to limit global temperature rises have increasingly focused
52 attention on reducing methane emissions. Mitigation efforts rely, in turn, on accurate national
53 emissions inventories to identify the economic sectors which contribute to anthropogenic
54 methane emissions. Current best estimates indicate that the energy and agriculture sectors
55 respectively produce 30% and 36% of annual methane emissions in the United States
56 (Maasakkers et al., 2016). Reducing uncertainty in the contributions from these two sectors is
57 pressing but also quite challenging. Energy infrastructure and agricultural lands are often
58 comingled; at a typical inventory model resolution of 0.1°, we estimate that up to half of all areas
59 in the U.S. contribute both energy and agriculture sector methane fluxes. Observational studies
60 must overcome this collocation challenge to constrain the magnitude and distribution of methane
61 emissions from these two sectors.

62

63 Here, we present results from a multi-month study in the Northern Colorado Front Range Urban
64 Corridor which demonstrate direct, sector-sepcific inventory optimizations by combining novel
65 instrumentation and analytical methods. Methane emissions in this region arise predominantly
66 from the energy and agriculture sectors; rapidly expanding energy infrastructure in the Denver-
67 Julesburg Basin (DJB) over the past two decades has become increasingly intermingled with
68 areas where livestock are raised (Fig 1a, Fig 1b). Multi-month data sets of methane, ethane, and
69 ammonia mixing ratios (Fig 1c) were collected at a regional site using a cavity ring-down
70 spectrometer and, for the first time, an open-path, mid-infrared dual-comb spectrometer (MIR-
71 DCS). The broad spectral bandwidth of the MIR-DCS instrument enables multi-species
72 quantification, which in turn is critical for sector apportionment of methane (Coddington et al.,
73 2016; Giorgetta et al., 2021; Ycas et al., 2018). From these observational data, we construct a
74 dynamic linear model framework which extends the application of tracer gas sector attribution to
75 the long duration of the observational data (Kille et al., 2019; Pollack et al., 2022; Yacovitch et
76 al., 2014, 2015) In combination, the dual-comb spectroscopy technique and dynamic linear
77 model analysis provide crucial information that constrains the regional distribution of energy and
78 agriculture methane fluxes. Sector-resolved inventory models are compared to observations and
79 optimized using a Bayesian inverse method. Posterior energy emissions in the region are similar
80 to 2012 inventory estimates despite a ~360% increase in energy production; this corroborates
81 other studies hypothesis that emissions factors have changed since the inventory was constructed
82 (Peischl et al., 2018). Agricultural methane fluxes were 3× greater than inventory estimates; we
83 demonstrate that this discrepancy arises from the spatial concentration of livestock which is not
84 captured in the inventory model. Sector-resolved inventory evaluations presented here
85 demonstrate how complex regional emissions inventories can be verified using a combination of

86 instrumental and analytical techniques. The intrinsic sector sensitivity of this approachcould be
87 broadly implemented across much larger regions andfills gaps in our understanding of national-
88 and global-level methane emissions from different economic sectors.
89
90
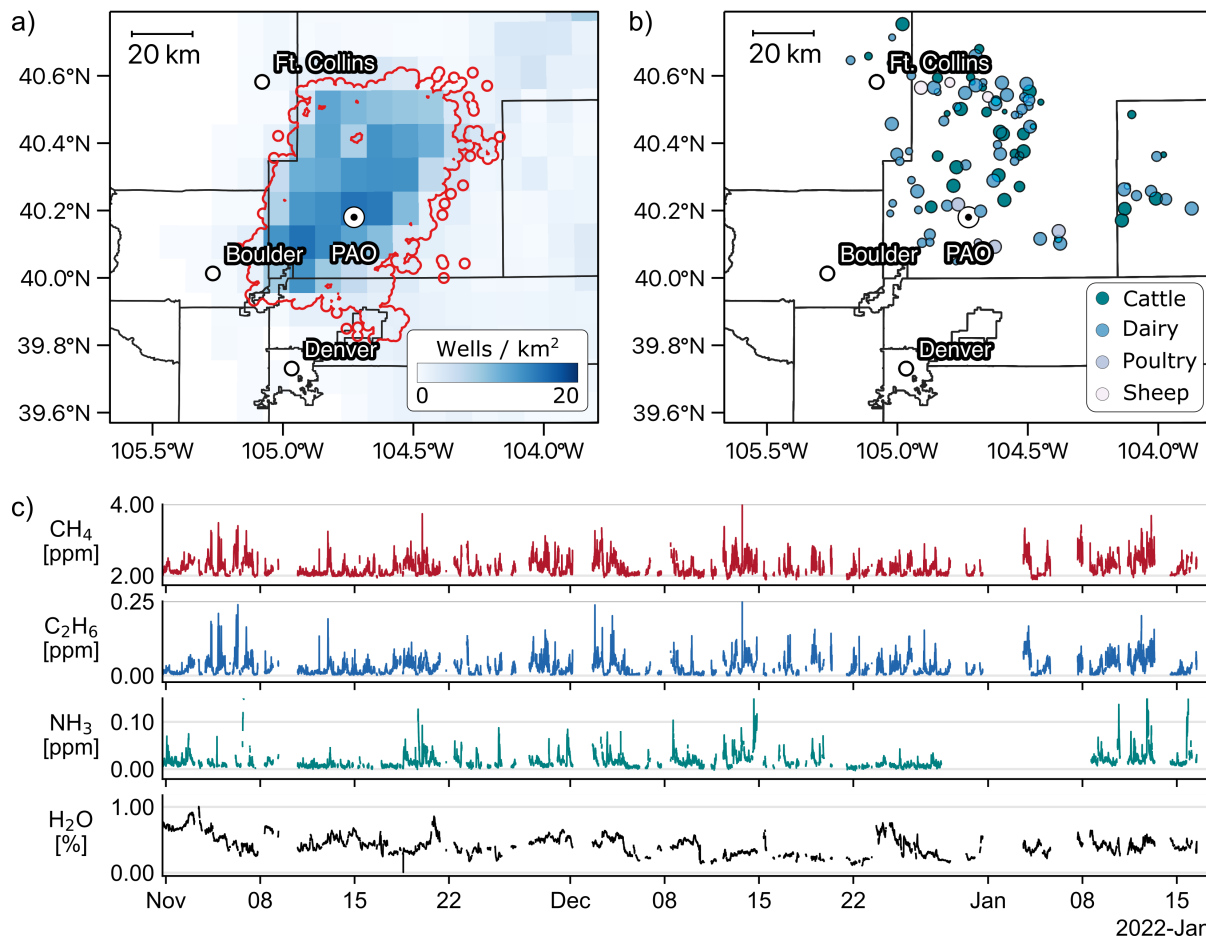
Figure 1 a) The Front Range Urban Corridor extends along the eastern edge of the Rocky Mountains. Tens of thousands of wellheads (shown as a density map) installed in the region extract oil and gas from the Wattenberg field (red outline). County outlines are shown in black. Data were collected at the Platteville Atmospheric Observatory (PAO). b) Agricultural activities, such as confined animal feeding operations (CAFO, color coded by livestock and scaled to relative expected emissions magnitude), are widely distributed and spatially overlapped with energy infrastructure. c) Full methane, ethane, ammonia, (expressed as dry mixing ratios) and water time series recorded at PAO, over the 2.5 month period by an open-path, mid-infrared dual-comb spectrometer for methane, ethane and water, and by a cavity ringdown spectrometer for ammonia.

2 Materials and Methods

2.1 Observational data collection

Measurements collected at the Platteville Atmospheric Observatory (PAO) from 1 November 2021 to 17 January 2022 are used in this analysis. Methane (CH_4), ethane (C_2H_6), and

107 water (H_2O) concentrations were measured with an open-path mid-infrared (MIR) dual-comb
108 spectrometer (DCS), while ammonia (NH_3) was measured using a cavity ring-down spectrometer
109 (CRDS). Fig 1c shows the full CH_4, C_2H_6, and NH_3 time series expressed as dry air mole
110 fractions, reported in ppm [umol/mol] and/or ppb [nmol/mol]. Both instruments were
111 simultaneously sampling ~50% of the time; all analysis will rely on these overlapping periods.
112 Additional meteorological data (air temperature, pressure, relative humidity, solar radiation,
113 wind speed and direction) were obtained from a monitoring station run by the National Oceanic
114 and Atmospheric Administration (NOAA, station code PVL). A map of the measurement site is
115 provided in Fig S1.

116
117 The MIR DCS system is similar to previously reported designs (Giorgetta et al., 2021; Ycas et
118 al., 2019, 2020) and is described in more detail in (Herman et al., 2023). Briefly, the instrument
119 measures an optical bandwidth spanning 3-5 µm with 200-MHz spectral resolution.
120 Measurements extended along a 380-meter open-air path (760 m round trip) at an average height
121 above ground level of 5 meters to a retroreflector. The retroreflected light is collected with the
122 same transmit/receive telescope, detected by a thermoelectrically cooled mercury cadmium
123 telluride detector, digitized at 200 MHz, and coherently averaged to yield one atmospheric
124 spectra every 2 minutes (Roy et al., 2012; Ycas et al., 2018). These atmospheric transmission
125 spectra were fit to reference spectra from HITRAN2020 (Gordon et al., 2022) to retrieve the
126 path-averaged concentrations of CH_4, C_2H_6, and H_2O. Other species, including propane, heavier
127 alkanes and aromatic compounds are also present in the data but not analyzed here.

128
129 ## 2.2 Tracer gas analysis

130
131 Methane observations are modelled as the sum of energy emissions ($\beta_1 C_2 H_6$), agricultural
132 emissions ($\beta_2 NH_3$), a background term, β_0, and a Gaussian noise term ϵ (Kille et al., 2019):

133
134 $$CH_4 = \beta_0 + \beta_1 C_2 H_6 + \beta_2 NH_3 + \epsilon$$

135
136 where the dry mixing ratio is indicated by the chemical compound. This is appropriate for the
137 Front Range Urban Corridor where energy and agriculture contribute a majority of methane
138 emissions. Landfills can also provide a substantial methane flux and unfortunately have no
139 convenient distinguishing tracer gas. However, all major landfills are well outside our area of
140 sensitivity and therefore are not expected to contribute significantly.

141
142 The regression coefficients β_0, β_1, and β_2 are expected to vary throughout the duration of
143 observations at PAO since the background methane β_0 will surely change and the ratio of
144 methane to the tracer gases (β_1, and β_2) will also vary with the specific source. A static linear
145 regression approach will fail to capture this variation inherent to the multi-month time series. To
146 accommodate variations in the coefficients, we use a dynamic multivariate linear model. (West
147 & Harrison, 1997). Dynamic linear models (DLMs) consist of an observation equation

148
149 $$Y_t = F_t' \theta_t + v_t, \qquad v_t \sim N[0, V_t]$$

150
151 and a system equation

152

$$\theta_t = \theta_{t-1} + \omega_t, \qquad \omega_t \sim N[0, W_t]$$

Here, Y_t is the methane concentration at observation time point t, which has a Gaussian noise term ν_t with a mean of zero and a variance V_t (defined here as the variance of the point-wise difference of the methane time series). Tracer gas observations, along with a constant term which models the intercept, are included in the regression vector $F_t = (1_t, C_2H_{6,t}, NH_{3,t})$. The regression state vector $\theta_t = (\beta_{0,t}, \beta_{1,t}, \beta_{2,t})$ evolves over time as a function of the previous parameter vector and the evolution variance matrix W_t. Because this variance matrix is difficult to directly estimate and may not be time-invariant, DLMs are often solved using a discount factor δ instead as a proxy for the "memory" of the system over time (West & Harrison, 1997). The discount factor is defined as $\delta = P_t / (W_t + P_t)$, where P_t is the prior variance corresponding to a state vector with zero stochastic change ($W_t = 0$). In that limiting case, $\delta = 1$ (irrespective of the actual value of P_t) and the DLM is identical to a static multivariate regression model. An optimal discount factor can be determined through minimizing the model's mean standard error, but in practice this minimization becomes expensive for large data sets. For analysis in this work, replicates of the DLM were fit to the data using a random selection of discount factors spanning [0.98, 0.999]. Values below 0.98 were found to lead to numerical instability. (Note that data points where the variance of either β_1 or β_2 was greater than 100% of the fit value are excluded in subsequent analysis.)

2.3 Emissions inventories

This work considers a 0.1°×0.1° spatially gridded methane surface flux map derived from the 2012 EPA national methane inventory (Maasakkers et al., 2016). These estimates may be convolved with STILT-R influence footprints to predict sector-apportioned methane mixing ratios at PAO which can be used as priors for Bayesian inversions. The inventory relies on models of the size and spatial distribution of methane sources to generate sector-specific surface flux estimates. Annual sectoral estimates for emissions arising from energy production (1B2b (Natural Gas Production + Processing + Transmission + Distribution) + 1B2a (Petroleum)) and animal husbandry (4A (Enteric Fermentation) + 4B (Manure Management)) were used in this work.

2.4 Atmospheric dispersion modelling

A dispersion model is required to connect the measured sector-apportioned methane to an inventory. For this, we retrieve 3-km High Resolution Rapid Refresh (HRRR) meteorological data provided by the National Oceanic and Atmospheric Administration's Air Resources Laboratory. Based on these data and using the STILT-R Lagrangian transport model (Benjamin et al., 2016; Fasoli et al., 2018; Lin, 2003), we calculated hourly footprints over an 8 week period of observations spanning November and December 2021 spanning +/-3° latitude and longitude centered on PAO. These influence footprints were based on 24 hour and 48 hour back trajectories originating from PAO calculated at 1-hour steps using 100 particles at 0.1° resolution with hyper near field effects enabled. This influence footprint $f(\mathbf{x_r}, T_r \mid \mathbf{x_i}, T)$ (units of [ppm m^2 s / μmol CH$_4$]) connects emissions throughout the spatial domain, at location $\mathbf{x_i}$ and time T, to observed mixing ratios at PAO, at location $\mathbf{x_r}$ and time T_r. A "forward" estimate (prior prediction) of the tracer concentration change at the receptor due to transport from an emission source can be calculated by multiplying the influence footprint with a surface flux estimate $F(\mathbf{x_i},$

198 T) (units of [μmol CH$_4$ / m^2 s]) provided by the inventory, followed by summation over the
199 spatial domain of the simulation.
200
201 **2.5 Bayesian inversion**
202 From the observed energy and agriculture apportioned methane time series and back trajectory
203 simulations, we calculate maximum a posteriori (MAP) estimates $\hat{\mathbf{x}}$ and corresponding posterior
204 error covariance matrices $\hat{\mathbf{S}}$ for both sectors using the respective emissions inventory as the prior
205 estimate, $\mathbf{x_A}$ (Cusworth et al., 2020),

$$\hat{\mathbf{x}} = \mathbf{x_A} + \mathbf{SH^T}(\mathbf{HSH^T} + \mathbf{R})^{-1}(\mathbf{y} - \mathbf{Hx})$$

$$\hat{\mathbf{S}} = (\mathbf{H^T R^{-1} H} + \mathbf{S^{-1}})^{-1}$$

211 Observational time series were converted from two-minute to one-hour mean values; only
212 databetween hours 11-16 local time (when the boundary layer is assumed to be well mixed and at
213 a maximum height) were used in the analysis (Kunik et al., 2019). Optimization of the prior and
214 observational error covariance matrices R and S is discussed in the SI (Michalak?). The
215 averaging kernel sensitivity matrix, calculated from $\hat{\mathbf{S}}$, indicates the posterior estimate is
216 optimized across an area of 850 km^2 centerd around PAO. This region is highlighted with a
217 rectangular outline in Figs 4 and 5. The study's averaging kernel matrix is shown in Fig S5.
218

219 **3 Time-resolved Sector Apportioned Methane**

220 The dynamic linear model was applied to the full time series data. Significant day-to-day
221 variations in relative contributions from agriculture and energy were observed, consistent with
222 the complex regional source environment. Three illustrative examples are shown in Fig 2.
223 Methane, ethane, and ammonia mixing ratios, and DLM regression coefficients with
224 uncertainties are shown for time periods spanning 9-24 hours. Notably, the DLM regression
225 captures how uncertainty in the regression coefficients varies over time. During periods with a
226 low tracer gas mixing ratio or little variation in the tracer gas, uncertainty in the respective
227 regression coefficient increases. A sharp increase in one tracer gas concentration rapidly shrinks
228 the uncertainty in the respective DLM coefficient.
229
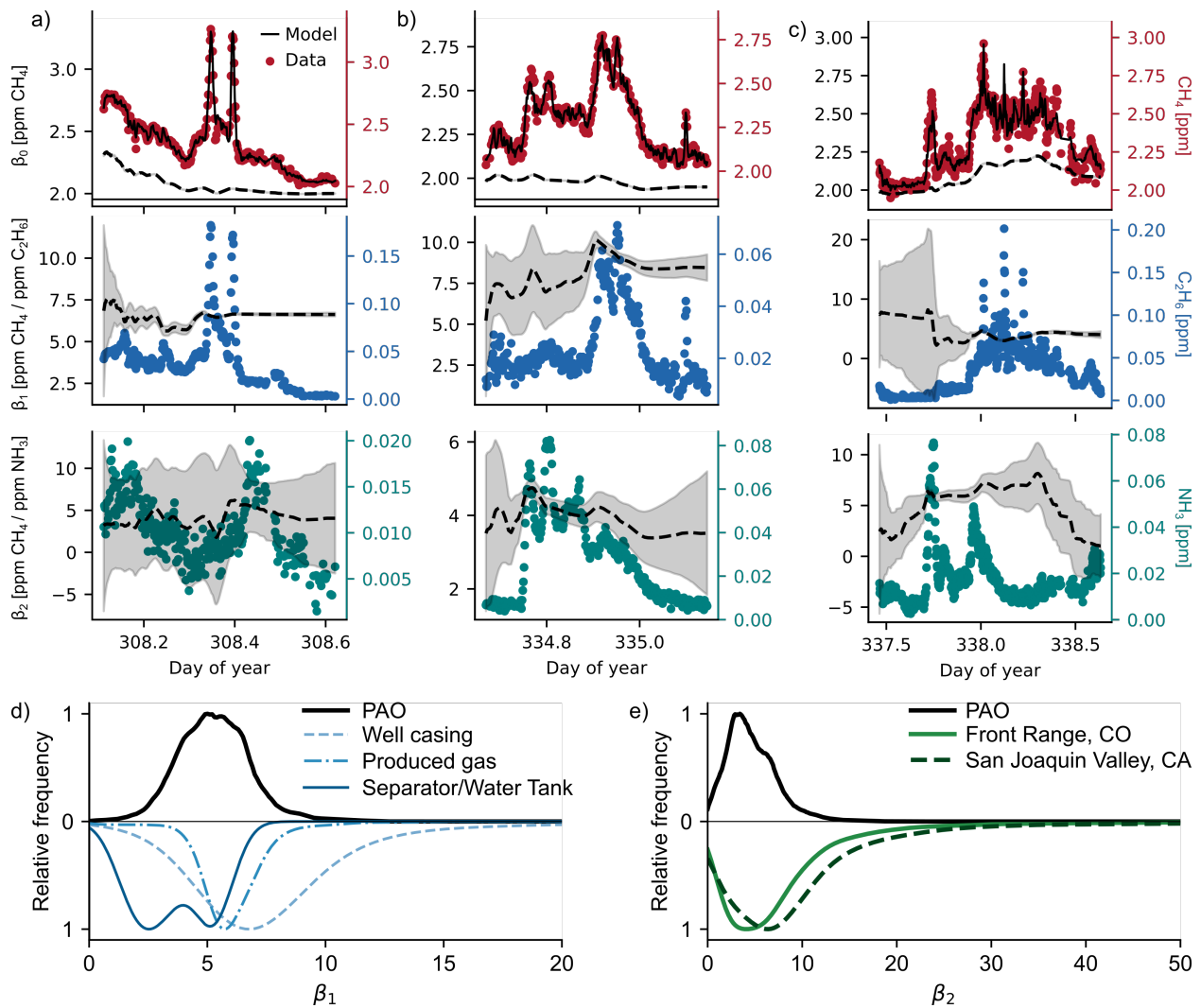
Figure 2 Three plume events illustrate how the dynamic linear regression model reproduces observed CH₄ dynamics. The three regression coefficients calculated using the dynamic linear model (dashed lines, left axis) are shown, with the uncertainty in gray shading. In addition, the top panel shows both the full modeled methane concentration (solid line, right axis) and the measured methane concentration (green circles, right axis). The second and third rows show the sector-apportioned methane for the energy and agricultural sectors respectively, based on the product of the tracer gas measurements and retrieved enhancement ratios (colored dots, right axis). Note that the enhancement ratios with the tracer gases, β_1 and β_2, cover a wide range of values, which highlights the usefulness of the DLM approach for resolving complex dynamics. Comparison of the enhancement factors retrieved from the DLM to other literature and available data. d) The range of β_1 coefficients observed at PAO are similar to coefficients calculated from COGCC sampling data. Evidence for produced gas emissions are apparent in the DLM results. e) β_2 coefficients at PAO are consistent with other studies performed in the Front Range Urban Corridor (Eilerman et al., 2016) and San Joaquin Valley (Miller et al., 2015).

Figure 2d-e shows kernel density estimate of the two enhancement ratios over the 2.5 month observation period. In the case of β_1, this ratio has been observed to vary as natural gas is

248   extracted, processed, and transported (Peischl et al., 2013). Ethane and methane mole fractions
249   for natural gas samples collected after 2010 in the Front Range Urban Corridor by the Colorado
250   Oil and natural gas Conservation Commission (COGCC) provided a direct comparison to our
251   estimates for β_1 (Fig 2d) (Colorado Oil and Gas Conservation Commission, 2022). COGCC
252   recorded data for a range of sample locations, including well casings, produced gas, and
253   separators and water tanks. For this analysis, well casings consisted of samples collected from
254   bradenheads, well tubing, and surface, intermediate, and production casings. The β_1 values
255   determined from the PAO data span the lower end of values for well casing and the higher range
256   of values for separator and water tank emissions, but are most consistent with produced gas
257   emissions.
258
259   Similarly, β_2 is expected to vary as emissions from chickens and cows can have substantially
260   different ratios of methane and ammonia concentrations (Golston et al., 2020). Other sources of
261   variation could include atmospheric chemical effects such as deposition and reactivity (primarily
262   for NH$_3$). We compare our β_2 results with two mobile measurement studies in Fig 2e. While
263   extensive studies examining ammonia/methane enhancement ratios are not available, studies in
264   both the San Joaquin Valley of California and the Front Range Urban Corridor in Colorado
265   overlap well with β_2 results obtained at PAO, indicating a consistent, if broad, distribution of
266   β_2 values for agriculture across the western United States (Eilerman et al., 2016; Miller et al.,
267   2015).
268
269   This analysis emphasizes that enhancement ratios are far from universal—even for a single
270   location—and that it is likely impossible to determine a unique set of β parameters for energy
271   and agriculture emissions even for a measurement spanning several hours. In the same vein,
272   descriptions of the relative fractions of agriculture- and energy-sector methane will vary based
273   upon the time period considered.

4 Comparison with inventories

275   We now compare sector-apportioned methane to inventory predictions using the "forward"
276   model (prior prediction) discussed in Section 2.4. The degree of agreement presumably reflects
277   the extent to which the inventory correctly models the real world methane sources. We can then
278   improve inventory agreement by generating a posterior estimate using a Bayesian inversion with
279   the inventory as the prior estimate. We consider only midday observations when the boundary
280   layer is on average well mixed and well approximated in the meteorological models. Figure 4a
281   and 5a summarizes the results for the energy and agricultural sector respectively. The
282   observation uncertainties were estimated with a bootstrap method by randomly sampling 20% of
283   the sector apportioned methane time series 500 times, calculating the hourly mean for each
284   sample, and calculating the variance of the spread of the hourly means. The uncertainty in the
285   forward model mixing ratios were based on the sector-dependent uncertainties described in
286   Maasakkers. Finally, the posterior uncertainties were calculated using the posterior error
287   covariance matrix (see SI).
288
289
290
291

293
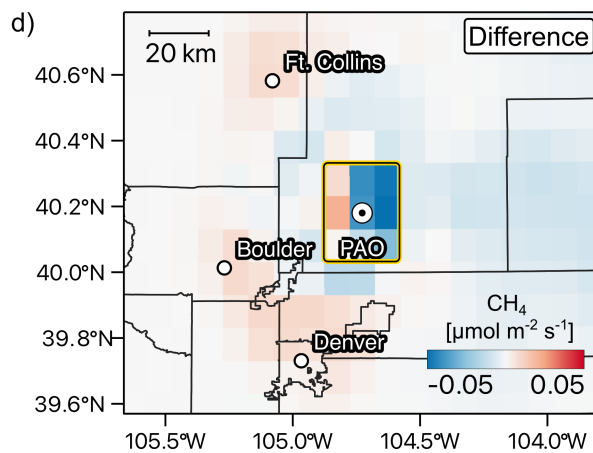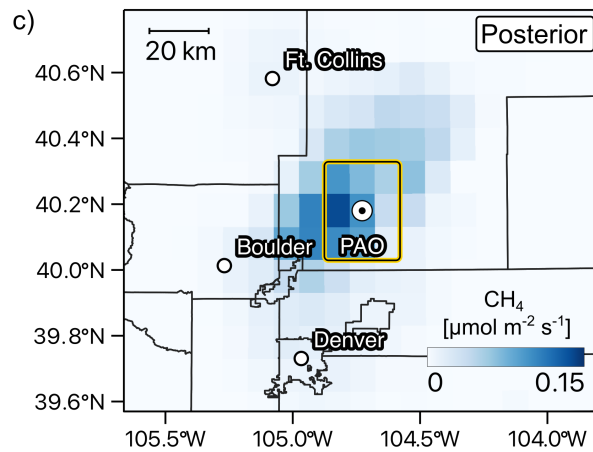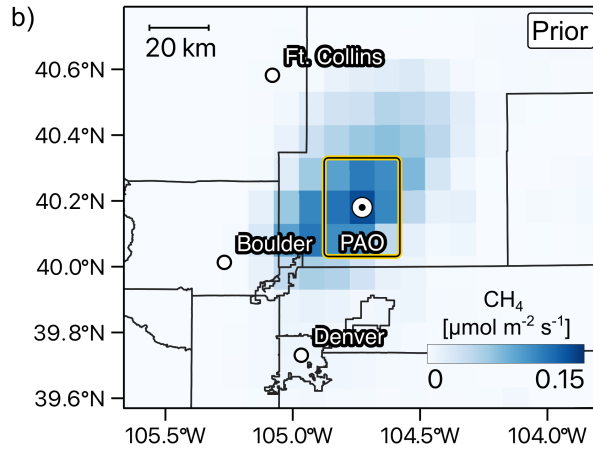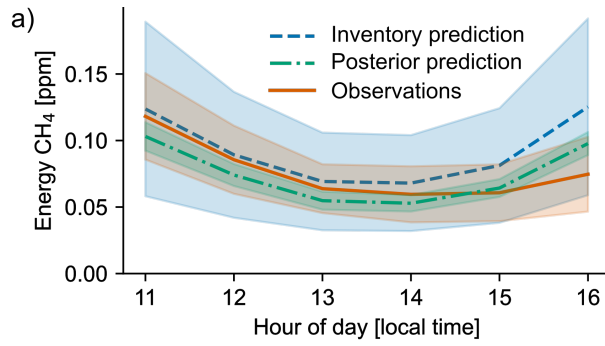
Figure 3 Comparison of energy-sector methane observed at PAO to the inventory and posterior
predictions. a) Midday mixing ratios observed at PAO are compared to forward model predictions
and the optimized Bayesian posterior. b-c) Prior and posterior surface flux maps for energy sector
methane emissions remain largely similar in both distribution and magnitude of emissions. d)
Difference between prior and posterior emissions are slight, with a general reduction in emissions
to the north-east of PAO.

4.1 Energy inventory

As shown in Figure 4a, there is good agreement between energy sector observations and
predictions. Hourly mean differences between observations and the prior and posterior were -
16.3 ± 55.0 ppb and 2.0 ± 25.8 ppb respectively. Within the region of high sensitivity (yellow
box centered on PAO) mean energy fluxes were 22% lower in the posterior solution (78.4 ± 3.5
nmol CH_4 m^{-2} s^{-1}) compared to the prior model (100.0 ± 53.0 nmol CH_4 m^{-2} s^{-1}). The Bayesian
inversion weights emissions in the posterior state vector slightly towards the west of PAO (Fig
4b), but overall there is little change in the posterior distribution relative to the prior

It is somewhat surprising that our observations from the winter of 2021-2022 are in close
agreement with the prior based on a 2012 inventory. PAO is in Colorado's Weld County, which
historically has produced the vast majority of oil and natural gas in Front Range Urban Corridor.
From 2012 to 2021, reported Weld County oil and natural gas production volumes increased by
factors of 370% and 360% respectively [COGCC], although the distribution of production across
the DJB became more localized and heterogeneous (Fig S4). The agreement between
observations and inventory suggests either that 1) 2012 emissions factors were over-estimated by
~3.6× , 2) emissions factors have declined since 2012, or 3) production within the region
aroundPAO remained unchanged relative to 2012.

Using an annual, spatially gridded dataset on oil and gas production volumes and new well
installations recently published by the USGS, we address these three possibilities (Skinner et al.,
2022). Case 3 was rejected since the mixing rations were predicted to increase several fold based
on the changes in the spatial inventories. Cases 1 and 2 are more interesting. The USGS data
indicate a significant change in well infrastructure and production trends since 2012. Between
2010-2012, horizontal drilling skyrocketed to become a ubiquitous technology for new well
installations; large increases in oil and natural gas production began shortly after. Given the
significant changes in both well infrastructure and extraction efficiency, we speculate that
emissions factors of horizontal well are substantially different than those used in the inventory
model. For example, the consolidated infrastructure at new sites could contribute to higher rates
of successful leak detection and repair than traditional vertically drilled single well installations
(Robertson et al., 2017). Adoption of more stringent state air quality standards in 2014 may have
further contributed to mitigate fugitive emissions from the energy sector. Indeed, other studies
are consistent with declining emission factors. Previous estimates from the DJB using aircraft
mass-balance flights [Petron, Peischl, Cusworth] have remained statistically unchanged from
2008 to 2021. Together, these data suggest that emissions factors were likely accurate for the
2012 inventory, and have likely decreased in the DJB since 2012 due to a combination of
regulations and changes in resource extraction.
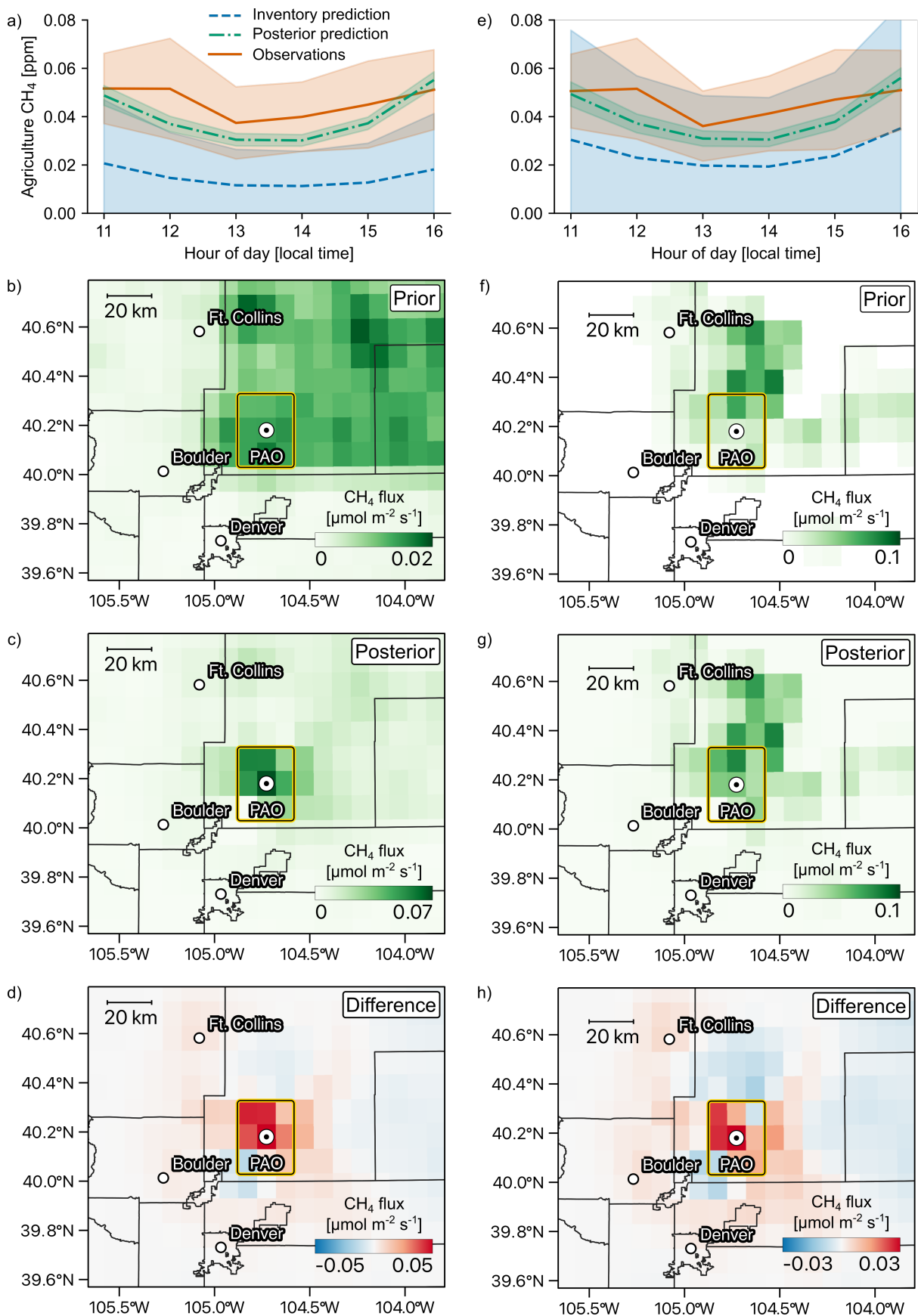
339

340 *Figure 4 Comparison of agriculture-sector methane observed at PAO to the original inventory*
341 *and posterior predictions (left column), and to the re-distributed inventory and posterior*
342 *predictions (right column). a) Midday mixing ratios observed at PAO are compared to inventory*
343 *and optimized Bayesian posterior predictions. b-c) Prior and posterior surface flux maps for*
344 *agriculter sector methane emissions demonstrate large differences, with the posterior emissions*
345 *more strongly localized around PAO. d) Difference between prior and posterior emissions are*
346 *significant, with a several-fold increase in emissions to the north-west. e) Comparison of*
347 *observations to the re-distributed agriculture inventory and the posterior predictions. Agriculture*
348 *emissions uncertainties from Maasakkers were applied to calculate uncertainties in the*
349 *redistributed emissions map. f-g) The re-distributed prior and posterior are minimally different,*
350 *suggesting that the re-distribution better captures the actual distribution of emissions around*
351 *PAO. h) Differences between the re-distributed prior and posterior are slight, with adjustments on*
352 *the 50% level.*

353 ## 4.2 Agriculture inventory

354 In contrast to the energy sector, observed agriculture mixing ratios were on average $3.1\times$
355 larger than inventory predictions. The posterior reduces the mean hourly difference between
356 prior and observations from 31.3 ± 25.3 ppb CH_4 to 6.3 ± 16.7 ppb CH_4, largely by localizing
357 methane flux around PAO (Fig 5d). Agriculture mean methane fluxes increased within the region
358 of maximum sensitivity by $3\times$ from 13.68 ± 16.37 nmol CH_4 m^{-2} s^{-1} to 41.41 ± 1.12 nmol CH_4 m^{-2}
359 s^{-1}. This result is surprising as agricultural emissions should have remained roughly constant
360 from 2012 to 2021 based on censuses of permitted livestock (unlike energy production that
361 increased threefold in volume during that time period). Nonetheless, the substantial increase in
362 posterior emissions suggests that some error is present in the agriculture inventory. Comparison
363 of the inventory to registered concentrated animal feeding operations (CAFOs) locations
364 demonstrates that inventory fluxes are not localized around CAFOs. The agricultural inventory
365 was generated by probabilistically distributing known county level livestock headcounts onto
366 agriculture zoned land in that county. For some livestock, such as beef cattle which graze in
367 pastures for parts of the year, this is a logical approach; however chickens and dairy cattle are
368 frequently localized CAFOs. This suggests a spatial misallocation of sources, instead of large
369 errors in emissions factors, might explain the discrepancy with observations.

370

371 To test the hypothesis that re-distributing emissions to CAFO locations will generate an
372 improved inventory, county-level methane emissions were extracted from the EPA inventory and
373 redistributed to the physical locations of CAFOs within each county, proportionate to the total
374 animal equivalent emissions units at each CAFO (Golston et al., 2020). Crucially, no changes to
375 the total county level emissions are made, which reflects our assumption that agricultural
376 emissions factors remained constant from 2012 to 2021. As shown in Fig 5e, the redistributed
377 agriculture inventory improves agreement with observations, although the observed mixing
378 ratios remain $1.87\times$ larger. The updated posterior calculated using the redistributed inventory as
379 a prior reduces the ratio between posterior and observed mixing ratios to $1.17\times$ and reduces mean
380 hourly difference to 5.6 ± 17 ppb CH_4. Mean emissions in the sensitivity region were 42.8 ± 1.9
381 nmol CH_4 m^{-2} s^{-1} which is indistinguishable to the posterior solution calculated using the original
382 EPA agriculture inventory.

383

5 Conclusions

We have presented a long-term, sector-apportioned study of methane emissions in the Front Range Urban Corridor. By combining a dynamic linear model tracer gas analysis with inverse modelling, we constrain methane emissions from multiple economic sectors in a ~850 km^2 region using data from a single measurement location. Prior and posterior energy sector methane emissions agreed well with observations, which is strongly suggestive of a decrease in energy infrastructure emissions intensity from 2012 to 2021 in the Front Range Urban Corridor region. Large changes in the distribution of agriculture emissions are consistent with localized emissions from CAFOs, a detail which is excluded from the inventory. While conclusions from our single-sensor study can be further improved with a spatially distributed sensor network, it is noteworthy that the measurement approach can already provide valuable ground-truth data of sector-resolved methane emission across areas comparable to the footprints of many methane observing satellites (Cusworth et al., 2021).

Open Research

AGU requires an Availability Statement for the underlying data needed to understand, evaluate, and build upon the reported research at the time of peer review and publication. Additionally, authors should include an Availability Statement for the software that has a significant impact on the research. Details and templates are in the <u>Availability Statement</u> section of the Data & Software for Authors Guidance. For physical samples, use the IGSN persistent identifier, see the <u>International Geo Sample Numbers</u> section.

417

418 **References**

419 Benjamin, S. G., Weygandt, S. S., Brown, J. M., Hu, M., Alexander, C. R., Smirnova, T. G., et

420   al. (2016). A North American Hourly Assimilation and Model Forecast Cycle: The Rapid

421   Refresh. *Monthly Weather Review*, *144*(4), 1669–1694. https://doi.org/10.1175/MWR-D-

422   15-0242.1

423 Coddington, I., Newbury, N., & Swann, W. (2016). Dual-comb spectroscopy. *Optica*, *3*(4), 414–

424   426. https://doi.org/10.1364/OPTICA.3.000414

425 Colorado Oil and Gas Conservation Commission. (2022, September 15). Oil and Gas Well

426   Analytical Data. Retrieved from

427   https://cogcc.state.co.us/documents/data/downloads/environmental/ProdWellDownLoad.

428   html

429 Cusworth, D. H., Duren, R. M., Yadav, V., Thorpe, A. K., Verhulst, K., Sander, S., et al. (2020).

430   Synthesis of Methane Observations Across Scales: Strategies for Deploying a Multitiered

431   Observing Network. *Geophysical Research Letters*, *47*(7).

432   https://doi.org/10.1029/2020GL087869

433 Cusworth, D. H., Bloom, A. A., Ma, S., Miller, C. E., Bowman, K., Yin, Y., et al. (2021). A

434   Bayesian framework for deriving sector-based methane emissions from top-down fluxes.

435   *Communications Earth & Environment*, *2*(1), 242. https://doi.org/10.1038/s43247-021-

436   00312-6

437 Eilerman, S. J., Peischl, J., Neuman, J. A., Ryerson, T. B., Aikin, K. C., Holloway, M. W., et al.

438   (2016). Characterization of Ammonia, Methane, and Nitrous Oxide Emissions from

439   Concentrated Animal Feeding Operations in Northeastern Colorado. *Environmental*

440   *Science & Technology*, *50*(20), 10885–10893. https://doi.org/10.1021/acs.est.6b02851

441   Fasoli, B., Lin, J. C., Bowling, D. R., Mitchell, L., & Mendoza, D. (2018). Simulating

442   atmospheric tracer concentrations for spatially distributed receptors: updates to the

443   Stochastic Time-Inverted Lagrangian Transport model's R interface (STILT-R version

444   2). *Geoscientific Model Development*, *11*(7), 2813–2824. https://doi.org/10.5194/gmd-11-

445   2813-2018

446   Giorgetta, F. R., Peischl, J., Herman, D. I., Ycas, G., Coddington, I., Newbury, N. R., & Cossel,

447   K. C. (2021). Open-Path Dual-Comb Spectroscopy for Multispecies Trace Gas Detection

448   in the 4.5–5 µm Spectral Region. *Laser & Photonics Reviews*, *15*(9), 2000583.

449   https://doi.org/10.1002/lpor.202000583

450   Golston, L. M., Pan, D., Sun, K., Tao, L., Zondlo, M. A., Eilerman, S. J., et al. (2020).

451   Variability of Ammonia and Methane Emissions from Animal Feeding Operations in

452   Northeastern Colorado. *Environmental Science & Technology*, *54*(18), 11015–11024.

453   https://doi.org/10.1021/acs.est.0c00301

454   Gordon, I. E., Rothman, L. S., Hargreaves, R. J., Hashemi, R., Karlovets, E. V., Skinner, F. M.,

455   et al. (2022). The HITRAN2020 molecular spectroscopic database. *Journal of*

456   *Quantitative Spectroscopy and Radiative Transfer*, *277*, 107949.

457   https://doi.org/10.1016/j.jqsrt.2021.107949

458   Herman, D., Mead, G., Giorgetta, F. R., Baumann, E., Malarich, N., Washburn, B. R., et al.

459   (2023). Open-path measurement of stable water isotopologues using mid-infrared dual-

460   comb spectroscopy.

461   Kille, N., Chiu, R., Frey, M., Hase, F., Sha, M. K., Blumenstock, T., et al. (2019). Separation of

462   Methane Emissions From Agricultural and Natural Gas Sources in the Colorado Front

463   Range. *Geophysical Research Letters*, *46*(7), 3990–3998.

464   https://doi.org/10.1029/2019GL082132

465 Kunik, L., Mallia, D. V., Gurney, K. R., Mendoza, D. L., Oda, T., & Lin, J. C. (2019). Bayesian

466   inverse estimation of urban CO2 emissions: Results from a synthetic data simulation over

467   Salt Lake City, UT. *Elementa: Science of the Anthropocene*, *7*, 36.

468   https://doi.org/10.1525/elementa.375

469 Lin, J. C. (2003). A near-field tool for simulating the upstream influence of atmospheric

470   observations: The Stochastic Time-Inverted Lagrangian Transport (STILT) model.

471   *Journal of Geophysical Research*, *108*(D16), ACH 2-1-ACH 2-17.

472   https://doi.org/10.1029/2002JD003161

473 Maasakkers, J. D., Jacob, D. J., Sulprizio, M. P., Turner, A. J., Weitz, M., Wirth, T., et al.

474   (2016). Gridded National Inventory of U.S. Methane Emissions. *Environmental Science*

475   *& Technology*, *50*(23), 13123–13133. https://doi.org/10.1021/acs.est.6b02878

476 Miller, D. J., Sun, K., Tao, L., Pan, D., Zondlo, M. A., Nowak, J. B., et al. (2015). Ammonia and

477   methane dairy emission plumes in the San Joaquin Valley of California from individual

478   feedlot to regional scales. *Journal of Geophysical Research: Atmospheres*, *120*(18),

479   9718–9738. https://doi.org/10.1002/2015JD023241

480 Peischl, J., Ryerson, T. B., Brioude, J., Aikin, K. C., Andrews, A. E., Atlas, E., et al. (2013).

481   Quantifying sources of methane using light alkanes in the Los Angeles basin, California:

482   SOURCES OF METHANE IN L.A. *Journal of Geophysical Research: Atmospheres*,

483   *118*(10), 4974–4990. https://doi.org/10.1002/jgrd.50413

484 Peischl, J., Eilerman, S. J., Neuman, J. A., Aikin, K. C., de Gouw, J., Gilman, J. B., et al. (2018).

485   Quantifying Methane and Ethane Emissions to the Atmosphere From Central and

486   Western U.S. Oil and Natural Gas Production Regions. *Journal of Geophysical Research:*

487   *Atmospheres*. https://doi.org/10.1029/2018JD028622

488 Pollack, I. B., McCabe, M. E., Caulton, D. R., & Fischer, E. V. (2022). Enhancements in

489   Ammonia and Methane from Agricultural Sources in the Northeastern Colorado Front

490   Range Using Observations from a Small Research Aircraft. *Environmental Science &*

491   *Technology*, *56*(4), 2236–2247. https://doi.org/10.1021/acs.est.1c07382

492 Robertson, A. M., Edie, R., Snare, D., Soltis, J., Field, R. A., Burkhart, M. D., et al. (2017).

493   Variation in Methane Emission Rates from Well Pads in Four Oil and Gas Basins with

494   Contrasting Production Volumes and Compositions. *Environmental Science &*

495   *Technology*. https://doi.org/10.1021/acs.est.7b00571

496 Roy, J., Deschênes, J.-D., Potvin, S., & Genest, J. (2012). Continuous real-time correction and

497   averaging for frequency comb interferometry. *Optics Express*, *20*(20), 21932–21939.

498   https://doi.org/10.1364/OE.20.021932

499 Skinner, C. C., Miller, R. F., Kinney, S. A., Gianoutsos, N. J., Gunther, G., & Shorten, C. M.

500   (2022). Aggregated Oil and Natural Gas Drilling and Production History of the United

501   States [Data set]. U.S. Geological Survey. https://doi.org/10.5066/P9UIR5HE

502 West, M., & Harrison, J. (1997). *Bayesian forecasting and dynamic models* (2nd ed). New York:

503   Springer.

504 Yacovitch, T. I., Herndon, S. C., Roscioli, J. R., Floerchinger, C., McGovern, R. M., Agnese, M.,

505   et al. (2014). Demonstration of an Ethane Spectrometer for Methane Source

506   Identification. *Environmental Science & Technology*, *48*(14), 8028–8034.

507   https://doi.org/10.1021/es501475q

508   Yacovitch, T. I., Herndon, S. C., Pétron, G., Kofler, J., Lyon, D., Zahniser, M. S., & Kolb, C. E.

509   (2015). Mobile Laboratory Observations of Methane Emissions in the Barnett Shale

510   Region. *Environmental Science & Technology*, *49*(13), 7889–7895.

511   https://doi.org/10.1021/es506352j

512   Ycas, G., Giorgetta, F. R., Baumann, E., Coddington, I., Herman, D., Diddams, S. A., &

513   Newbury, N. R. (2018). High-coherence mid-infrared dual-comb spectroscopy spanning

514   2.6 to 5.2 μm. *Nature Photonics*, *12*(4), 202–208. https://doi.org/10.1038/s41566-018-

515   0114-7

516   Ycas, G., Giorgetta, F. R., Cossel, K. C., Waxman, E. M., Baumann, E., Newbury, N. R., &

517   Coddington, I. (2019). Mid-infrared dual-comb spectroscopy of volatile organic

518   compounds across long open-air paths. *Optica*, *6*(2), 165–168.

519   https://doi.org/10.1364/OPTICA.6.000165

520   Ycas, G., Giorgetta, F. R., Friedlein, J. T., Herman, D., Cossel, K. C., Baumann, E., et al. (2020).

521   Compact mid-infrared dual-comb spectrometer for outdoor spectroscopy. *Optics Express*,

522   *28*(10), 14740–14752. https://doi.org/10.1364/OE.385860

523
524

525

526

527

528

529

530